

# InP/ZnS Nanocrystals: Coupling NMR and XPS for Fine Surface and Interface Description

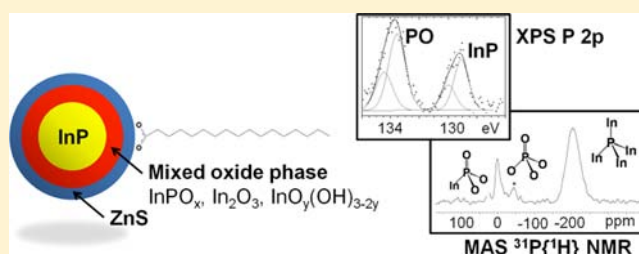
Héloïse Virieux,<sup>†</sup> Marianne Le Troedec,<sup>‡</sup> Arnaud Cros-Gagneux,<sup>†</sup> Wilfried-Solo Ojo,<sup>†</sup> Fabien Delpech,<sup>\*,†</sup> Céline Nayral,<sup>\*,†</sup> Hervé Martinez,<sup>\*,‡</sup> and Bruno Chaudret<sup>†</sup>

<sup>†</sup> Université de Toulouse; INSA, UPS, CNRS; LPCNO (Laboratoire de Physique et Chimie des Nano-Objets), 135 avenue de Rangueil, F-31077 Toulouse, France

<sup>‡</sup> Institut des Sciences Analytiques et de Physico-Chimie pour l'Environnement et les Matériaux, Université de Pau et des Pays de l'Adour, Hélioparc, 2 av. Président Angot, F-64053 Pau, France

## S Supporting Information

**ABSTRACT:** Advanced <sup>1</sup>H, <sup>13</sup>C, and <sup>31</sup>P solution- and solid-state NMR studies combined with XPS were used to probe, at the molecular scale, the composition (of the core, the shell, and the interface) and the surface chemistry of InP/ZnS core/shell quantum dots prepared via a non-coordinating solvent strategy. The interface between the mismatched InP and ZnS phases is composed of an amorphous mixed oxide phase incorporating InPO<sub>x</sub> (with *x* = 3 and predominantly 4), In<sub>2</sub>O<sub>3</sub>, and InO<sub>y</sub>(OH)<sub>3-2y</sub> (*y* = 0, 1). Thanks to the analysis of the underlying reaction mechanisms, we demonstrate that the oxidation of the upper part of the InP core is the consequence of oxidative conditions brought by decarboxylative coupling reactions (ketonization). These reactions occur during both the core preparation and the coating process, but according to different mechanisms.



of oxidative conditions brought by decarboxylative coupling reactions (ketonization). These reactions occur during both the core preparation and the coating process, but according to different mechanisms.

## INTRODUCTION

Because of their unique size- and shape-dependent electronic and optical properties, semiconductor nanocrystals (NCs) (also called quantum dots, QDs) have received considerable attention for both fundamental and technological interests. Significant achievements have been obtained across many scientific disciplines, as exemplified by their use as biolabels, lasers, light-emitting diodes (LEDs), and solar cells.<sup>1</sup> These successes depend on the control of both the intrinsic characteristics (size, shape, composition, etc.) of the NCs and their surface state. Concerning the latter aspect, overcoating with a large-gap semiconductor results in superior properties, such as enhanced photoluminescence (PL), quantum yield (QY), and stability. These improvements are generally attributed to the passivation of the dangling bonds at the core/shell (C/S) interface in combination with the confinement of the exciton in the core.<sup>2</sup> Additionally, in recent years, it became clear that the details of the atomic landscape at the C/S interface (i.e., abrupt- or graded-composition interfacial region) also have a dramatic influence on the optoelectronic properties. An example is the suppression of blinking phenomenon in graded CdSe/ZnSe QDs, while the corresponding abrupt C/S QDs display the typical blinking behavior.<sup>3</sup> Therefore, further progress in optoelectronic engineering relies on a deep understanding and, thus, a thorough knowledge at the atomic scale of the structure and the composition of the core and of the shell, but also of the interfacial layers.

Considering the nanometer-scale dimension of QDs, determination of the elemental distribution represents a significant challenge that has attracted much effort in the past two years. Several strategies (HRTEM/HAADF-STEM study,<sup>4</sup> Raman spectroscopy analysis,<sup>5</sup> STEM-EELS or STEM-EDX<sup>3</sup>) have been developed to probe the C/S interface in ionic II–VI-type (and to a lesser extent IV–VI-type) semiconductors. However, it remains difficult to discriminate elements with similar atomic numbers and to characterize poorly crystallized samples. In this context, X-ray photoelectron spectroscopy (XPS) appears an interesting alternative that can be used successfully to detail the internal composition with an accurate in-depth resolution.<sup>6,7</sup>

In the case of InP QDs (one of the promising alternatives to the ubiquitous Pb- and Cd-based NCs,) which combine low intrinsic toxicity and size-tunable emission in the visible and near-infrared spectral range, the question of the interfacial region composition is not or only partially answered. These issues are all so important that robust and straightforward strategies to synthesize InP/ZnS QDs are now available<sup>8–12</sup> and have already led to significant achievements in applications in domains such as *in vivo* biolabels<sup>13</sup> and LEDs.<sup>14</sup> Despite these successes, a deep knowledge of this system is still lacking, and optical performance, in particular in terms of QY, remains inferior to those of their II–VI and IV–VI counterparts. The

Received: July 20, 2012

Published: November 6, 2012

most significant accomplishment in terms of InP/ZnS compositional characterization was obtained by Reiss et al. on QDs prepared with indium carboxylate and  $\text{PH}_3$  as indium and phosphorus sources.<sup>10,11</sup> They showed through a detailed XPS study that, according to the synthetic procedures, different internal structures are obtained. The interpretation of the data was based on the assumption of the absence of oxide (thanks to inert atmosphere during synthesis).<sup>15</sup> However, we have recently demonstrated that, even so, oxide can be formed. Indeed, the synthesis of InP NCs using carboxylate precursors under inert atmosphere results in partial oxidation of the InP surface due to a side reaction involving the carboxylate capping ligands.<sup>16</sup>

In this article, we report a comprehensive overview on InP/ZnS NCs and, in particular, the in-depth compositional characteristics of the organic coating, the shell, and the core, as well as the C/S interface of InP/ZnS. Our strategy relies on the use of advanced multinuclear solution- and solid-state NMR and XPS as complementary techniques for unambiguous assignments. Both techniques are, indeed, well-suited for discriminating species, but they also provide radial descriptions of QDs.<sup>15–17</sup> The results described below will, on one hand, reveal the elemental distribution within the NCs and, on the other hand, show that a coating procedure involving zinc carboxylate and sulfur must not be considered as innocent (as initially expected) for the nature of the core, which is further oxidized during the coating step.

## EXPERIMENTAL SECTION

**Chemicals.** Indium acetate ( $\text{In}(\text{OAc})_3$ , 99.99%), palmitic acid (99.0%), elemental sulfur (99.98%), zinc undecylate (99.99%), and 1-octadecene (ODE, 90%, technical grade) were purchased from Sigma-Aldrich. Tris(trimethylsilyl)phosphine ( $\text{P}(\text{TMS})_3$ , 98.0%) was purchased from Strem. Toluene and acetone (RPE, analysis grade) were purchased from Carlo Erba. All reagents and solvents were dried, distilled, and degassed before use by using three freeze–pump–thaw cycles. All manipulations were carried out under an argon atmosphere using Schlenk tubes and vacuum line techniques, or in a glovebox. InP NCs were synthesized according to a previously described procedure.<sup>8,16</sup>

**Synthesis of InP/ZnS Nanocrystals.** To 10 mL of the dark red-brown crude InP solution is added 10 mL of ODE. To this solution, 0.56 mmol (243 mg) of zinc undecylate with 8 mL of ODE, and 0.56 mmol (19.2 mg) of elemental sulfur with 6 mL of ODE, are injected at 150 °C. The system is heated to 220 °C for 30 min. The solution becomes dark red and is cooled to room temperature. Isolation is done by following the purification procedure: the crude reaction solution is mixed with 3 equiv volume of acetone and centrifuged (18 000 rpm) for 20 min. The supernatant is discarded. The red precipitate is dispersed in 1 mL of toluene, and 10 mL of acetone is added, giving a cloudy solution that is centrifuged (18 000 rpm) for 10 min. The red precipitate is washed three more times following the same procedure and then dried under reduced pressure.

**Transition Electronic Microscopy.** Samples for TEM analysis were prepared in a glovebox by slow evaporation of a drop of the colloidal solution deposited onto a carbon-covered copper grid. TEM analysis were performed at the Service Commun de Microscopie Electronique de l'Université Paul Sabatier (TEMSCAN) on a JEOL JEM 1011 electron microscope operating at 100 kV with a point resolution of 4.5 Å. The size distributions were determined by measuring ca. 300 particles using Image J software.

**Nuclear Magnetic Resonance Spectroscopy.** 1D and 2D  $^1\text{H}$ ,  $^{31}\text{P}$ , and  $^{13}\text{C}$  NMR experiments in the liquid state were recorded on a Bruker Avance 500 spectrometer equipped with a 5 mm triple-resonance inverse Z-gradient probe (TBI  $^1\text{H}$ ,  $^{31}\text{P}$ , BB). The InP QDs concentration range used in the dispersions is  $1 \times 10^{-4}$ – $5 \times 10^{-4}$  M.

All the  $^1\text{H}$  and  $^{13}\text{C}$  signals are assigned on the basis of chemical shifts, spin–spin coupling constants, splitting patterns, and signal intensities, and by using  $^1\text{H}$ – $^1\text{H}$  COSY45,  $^1\text{H}$ – $^{13}\text{C}$  HMQC, and  $^1\text{H}$ – $^{13}\text{C}$  HMBC experiments. All diffusion measurements were made using the stimulated echo pulse sequence. The recycle delay was adjusted to 3 s. The strength of the gradient was calibrated by measuring the self-diffusion of the residual HDO signal in a 100%  $\text{D}_2\text{O}$  sample at 298 K ( $1.90 \times 10^{-9} \text{ m}^2 \text{ s}^{-1}$ ). For 2D diffusion-ordered spectroscopy (DOSY), after Fourier transformation and baseline correction, the diffusion dimension was processed with the Bruker Topspin software package. Solid-state NMR spectra were recorded on a Bruker Avance 400 spectrometer equipped with a 4 mm probe. Samples were spun at 7 kHz at the magic angle using  $\text{ZrO}_2$  rotors. For  $^1\text{H}$  magic angle spinning (MAS),  $^{13}\text{C}$  MAS, and  $^{31}\text{P}$  MAS single-pulse experiments, small flip angles ( $\sim 30^\circ$ ) were used with recycle delays of 5, 10, and 60 s, respectively.  $^{13}\text{C}$  cross-polarization (CP)/MAS and  $^{31}\text{P}$  CP/MAS spectra were recorded with a recycle delay of 5 s and contact times of 2 and 3 ms, respectively. All the  $^{13}\text{C}$  and  $^{31}\text{P}$  NMR spectra were recorded under high-power proton decoupling conditions. All chemical shifts for  $^1\text{H}$  and  $^{13}\text{C}$  are relative to TMS.  $^{31}\text{P}$  chemical shifts are referenced to an external 85%  $\text{H}_3\text{PO}_4$  sample.  $^{31}\text{P}\{^1\text{H}\}$  MAS NMR spectra were fully deconvoluted by dmfit software.<sup>18</sup>

**Fourier Transform Infrared Spectroscopy.** FT-IR spectra were recorded on a Nicolet 6700 FT-IR spectrometer.

**UV–Visible Absorbance Spectroscopy.** UV spectra were measured by using a Perkin-Elmer Lambda 35 scanning spectrophotometer with the samples in a 2 mm cell.

**Photoluminescence Spectroscopy.** PL spectra were acquired with a PTI Fluorescence Master System equipped with a xenon lamp ( $\lambda_{\text{excit}} = 400 \text{ nm}$ ).

**X-ray Diffraction Spectroscopy.** XRD spectra were recorded on a Panalytical spectrometer using  $\text{Co K}\alpha$  radiation. A powder of the sample was placed between two Kapton films for analysis.

**X-ray Photoelectron Spectroscopy.** The nanoparticles were characterized by XPS measurements carried out with a Kratos Axis Ultra spectrometer, using focused monochromatized  $\text{Al K}\alpha$  radiation ( $h\nu = 1486.6 \text{ eV}$ ). The XPS spectrometer was directly connected to an argon drybox through a transfer chamber, to avoid moisture/air exposure of the samples. For the  $\text{Ag } 3d_{5/2}$  line, the full width at half-maximum (fwhm) was 0.58 eV under the recording conditions. The analyzed area of the samples was  $300 \mu\text{m} \times 700 \mu\text{m}$  (large scale). Peaks were recorded with a constant pass energy of 20 eV. The pressure in the analysis chamber was  $\sim 5 \times 10^{-8} \text{ Pa}$ . Short acquisition time spectra were recorded before and after each normal experiment to check that the samples did not suffer from degradation under the X-ray beam during measurements. Peak assignments were made with respect to reference compounds analyzed under the same conditions (see Supporting Information, Figure S2, Tables S1 and S2). The binding energy scale was calibrated from hydrocarbon contamination using the C 1s peak at 285.0 eV. Core peaks were analyzed using a nonlinear Shirley-type background. The peak positions and areas were optimized by a weighted least-squares fitting method using 70% Gaussian, 30% Lorentzian lineshapes. Quantification was performed on the basis of Scofield's relative sensitivity factors.

## RESULTS AND DISCUSSION

**InP Core Characterization.** The InP NCs were synthesized following the straightforward procedure previously reported by Peng et al., with  $\text{In}(\text{OAc})_3$  and  $\text{P}(\text{TMS})_3$  as the indium and phosphorus sources in the presence of palmitic acid in ODE.<sup>8</sup> We have recently shown that this nanomaterial can be described as a core/multishell object. First, the NCs are composed of a crystalline InP core displaying a zinc-blende structure as previously reported in the literature.<sup>16</sup>  $^{31}\text{P}$  MAS NMR experiments show that compositional variations exist at and near the NCs surface. The QDs surface must be, then, considered as a partially oxidized zone including several chemical environments. A representative spectrum with

assignments is given in Figure 1, and shows the presence of  $\text{InPO}_4$  and  $\text{InP}$  resonances respectively at  $\delta -1$  and  $-195$  ppm

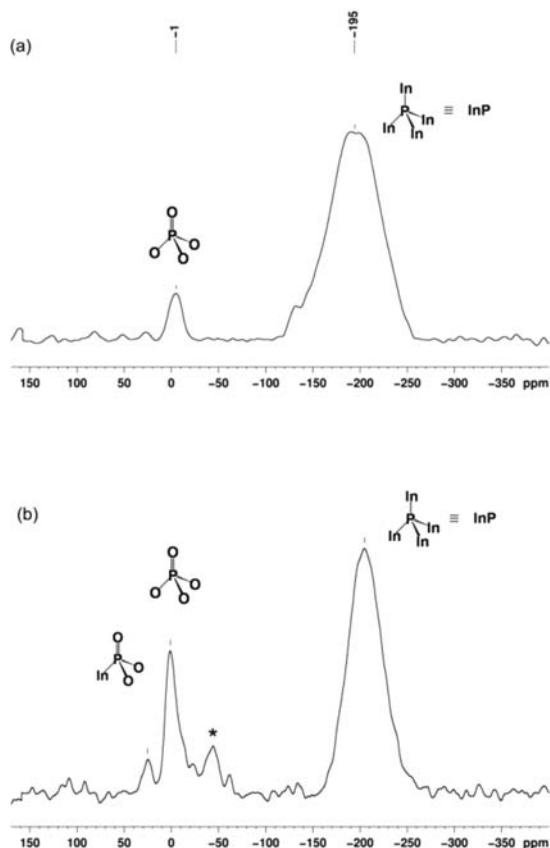
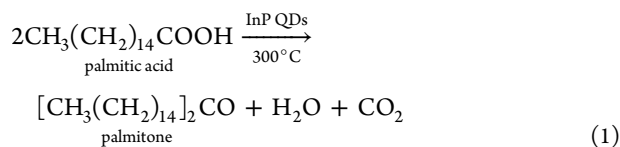


**Figure 1.**  $^{31}\text{P}\{^1\text{H}\}$  MAS NMR spectra of  $\text{InP}$  (a) and  $\text{InP}/\text{ZnS}$  (b) QDs (\*: spinning sideband).

with an intensity ratio of 8:92. The significant increase of intensity for the  $-1$  ppm resonance and the appearance of a new peak at  $\delta 22$  ppm (assigned to  $\text{InPO}_3$  species)<sup>16</sup> in the CP  $^1\text{H}-^{31}\text{P}$  MAS NMR spectrum (Figure S1) show unambiguously that these resonances arise from phosphorus species located at the surface. The CP sequence, indeed, allows us to infer spatial proximities between species at the surface, as it relies on dipolar through-space interactions coupling between different  $^1\text{H}$  spins (from the ligands) and  $^{31}\text{P}$  from the core. Second, the  $\text{InP}/\text{InPO}_x$  core is surrounded by an organic coating including residual solvent molecules, palmitate ligands, and a dialkyl ketone (palmitone).

This ketone is formed during the synthesis process via a decarboxylative coupling route (ketonization). The general equation of this reaction is given in eq 1. This reaction provides



oxidative conditions, presumably through the *in situ* generation of water, which leads to the conversion of the top layer of  $\text{InP}$  QDs into  $\text{InPO}_x$ .<sup>16</sup> Thorough washing of  $\text{InP}$  QDs gets rid of palmitone, while trace amounts of ODE remain in the QDs coordination sphere.

These  $\text{InP}$  QDs were also analyzed by XPS. The  $\text{In } 3d$ ,  $\text{O } 1s$ ,  $\text{P } 2p$ , and  $\text{C } 1s$  core peaks as well as the Auger peak  $\text{M}_4\text{N}_{45}\text{N}_{45}^{19}$  are presented in Figure 2 (bottom), and the corresponding data are presented in Table 1.

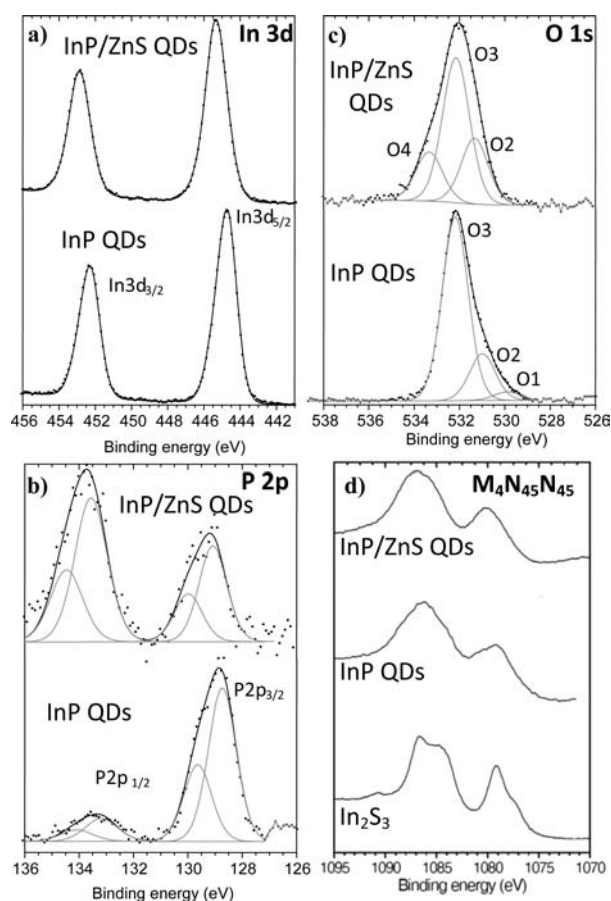


**Figure 2.** Comparison of  $\text{In } 3d$  (a),  $\text{P } 2p$  (b), and  $\text{O } 1s$  (c) spectra and Auger peak ( $\text{M}_4\text{N}_{45}\text{N}_{45}$ )<sup>19</sup> obtained for  $\text{InP}$  and  $\text{InP}/\text{ZnS}$  QDs and bulk  $\text{In}_2\text{S}_3$  (d).

First, we can note that the atomic percentage of carbon of  $\text{InP}$  QDs is high ( $\sim 80\%$ ) due to the presence of palmitic acid at the surface of these nanoparticles (Table 1). The  $\text{In } 3d$  spectrum exhibits two contributions,  $3d_{5/2}$  and  $3d_{3/2}$  (resulting from the spin-orbit splitting), located at respectively 444.7 and 452.2 eV (Figure 2a, bottom), which can be assigned to  $\text{InP}$ . The  $\text{P } 2p$  spectrum (Figure 2b, bottom) clearly evidences the presence of two chemical environments for phosphorus atoms. The spectrum has been fitted by considering two resolved doublets (with a spin-orbit splitting of  $\sim 0.9$  eV between  $2p_{3/2}$  and  $2p_{1/2}$ ). The first predominant doublet, present at 128.7–129.6 eV, is characteristic of  $\text{InP}$ . The second one, with a lower intensity, is located at higher binding energies, 133.2–134.1 eV, and corresponds, in agreement with the NMR results, to phosphorus in an oxidized environment, probably  $\text{InPO}_x$ .<sup>20</sup> The quantitative data obtained for  $\text{InP}$  QDs suggest an indium-rich surface (XPS atomic percentage reveals that  $\text{In}/\text{P}$  is close to 1.9), consistent with previous reports.<sup>11</sup> The  $\text{O } 1s$  spectrum (Figure 2c, bottom) allows identifying new indium-containing phases that could not be detected by NMR. Indeed, the peak present at 529.9 eV (O1 component) is characteristic of indium oxide,  $\text{In}_2\text{O}_3$ , as presented in Figure S2b (see Supporting Information), and the one at 531.1 eV (O2) corresponds to

Table 1. Quantitative Data from XPS Analysis<sup>a</sup>

C 1s		O 1s		In 3d		P 2p		S 2p		Zn 2p	
BE (fwhm)	at.%	BE (fwhm)	at.%	BE (fwhm)	at.%	BE (fwhm)	at.%	BE (fwhm)	at.%	BE (fwhm)	at.%
<b>InP</b>											
C1: 285.0 (1.0)	75.9	O1: 529.9 (1.3)	0.5	—	—	128.7–129.6 (1.2)	2.1	—	—	—	—
C2: 286.4 (0.9)	1.3	O2: 531.1 (1.3)	2.6	444.7–452.2 (1.2)	5.3	133.2–134.1 (1.4)	0.6	—	—	—	—
C3: 288.8 (1.2)	3.0	O3: 532.2 (1.3)	8.7	—	—	—	—	—	—	—	—
<b>InP/ZnS</b>											
C1: 285.0 (1.2)	55.1	O2: 531.3 (1.4)	4.1	—	—	129.0–129.9 (1.2)	0.9	161.4–162.6 (1.2)	7.6	1021.2–1044.3 (1.5)	6.9
C2: 286.5 (1.2)	4.1	O3: 532.1 (1.4)	7.5	445.4–452.9 (1.3)	3.0	133.5–134.4 (1.4)	1.7	161.9–163.1 (1.2)	2.4	—	—
C3: 288.9 (1.2)	3.6	O4: 533.3 (1.4)	3.1	—	—	—	—	—	—	—	—

<sup>a</sup>BE, binding energy (eV); fwhm, full width at half-maximum; and at.%, atomic percentage.

hydroxyls of indium hydroxide, InOOH or In(OH)<sub>3</sub>-types. The peak located at 532.2 eV (O3),<sup>21</sup> the predominant one, could be associated with oxygen of carboxylate function (in agreement with the C1s component (C3) located at 288.8 eV, Table 1) and with InPO<sub>x</sub>.<sup>22,23</sup> Finally, the two other components of the XPS C1s core peaks at 285.0 and 286.5 eV are assigned respectively to C–C and C–H bonds and to C–O bonds.

This information provides a complete overview and a detailed description of the chemical nature of the InP QDs prepared from indium carboxylate and P(TMS)<sub>3</sub>. Thus, these nano-objects must not be considered as a homogeneous InP phase but instead as a crystalline InP core surrounded by an amorphous mixed oxide phase incorporating InPO<sub>x</sub> (with  $x = 3$  and predominantly 4), InOOH, or/and In(OH)<sub>3</sub> as well as In<sub>2</sub>O<sub>3</sub> (Figure 3), on which palmitate ligands are tightly bonded.<sup>16</sup>

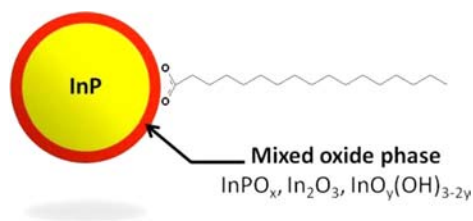


Figure 3. Graphical schematic representation of InP QDs.

### InP/ZnS NCs: Shell, Interface, and Surface Characterization.

The coating of InP NCs was achieved following the procedure previously reported by Peng et al. from zinc carboxylate and elemental sulfur.<sup>24</sup> As expected, the optical properties of the InP QDs were found to be dramatically modified, in particular with the high increase in the band edge luminescence intensity and the strong decrease of the surface defect emission (Figure 4). These features are fully consistent with the previous descriptions of InP/ZnS QDs prepared from indium and zinc carboxylate precursors, a procedure that is now well-established.<sup>9,11,24–26</sup> A representative TEM picture and a typical X-ray diffraction pattern of the zinc-blende phase of InP/ZnS are shown in Figure 4. In the latter analysis, the coating results in the shift of the diffraction peaks of InP toward the characteristic positions of cubic ZnS. The presence of sulfur and zinc in the XPS spectra (Figure 5 and Table 1) also gives evidence of coating. The quantitative data show Zn/S and Zn/In ratios of 1.4 and 2.3, respectively. These values are consistent with previous quantitative analysis of InP/ZnS QDs.<sup>9,25</sup>

Surprisingly, the shelling results in significant modifications of the <sup>31</sup>P MAS NMR spectra compared to that of the unshelled NCs (Figure 1). First, the <sup>31</sup>P{<sup>1</sup>H} MAS NMR spectrum clearly shows the significant increase of the ratio of oxidized phosphorus atoms (InPO<sub>3</sub>, InPO<sub>4</sub>), which almost triples (from 8% to 21%), while the one of In<sup>31</sup>P signal significantly decreases from 92% to 79% (Figure 1b). Second, concerning the In<sup>31</sup>P resonances, the line shape shows a significant narrowing (~30%) of the corresponding signal fwhm, 6800 Hz. This observation can be ascribed to the

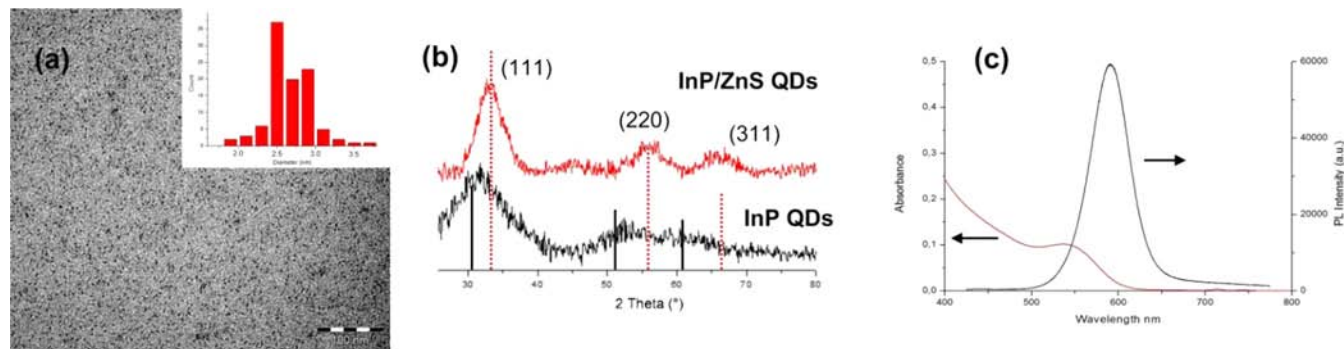
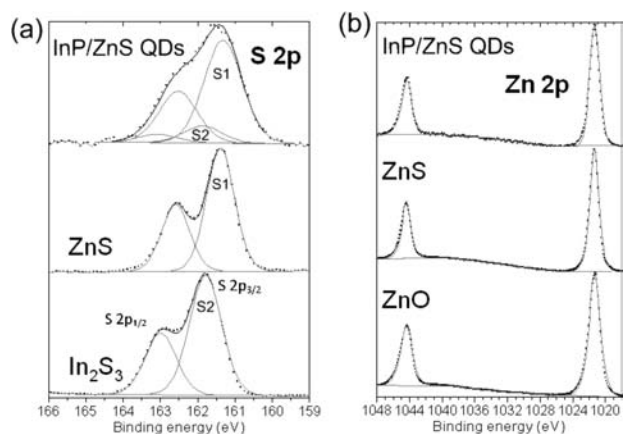


Figure 4. (a) TEM image, (b) X-ray diffractogram (solid and dotted lines respectively indicate InP and ZnS references), and (c) UV-vis and PL spectra of InP/ZnS QDs. The inset of panel a shows the size distribution of the InP/ZnS QDs.



**Figure 5.** Comparison of S 2p (a) and Zn 2p (b) spectra obtained for InP/ZnS QDs and the bulk references ZnS,  $\text{In}_2\text{S}_3$ , and ZnO.

reduction of the distribution of chemical shift when compared to non-coated InP NPs. Unshelled NPs indeed display a manifold of chemical environments at the surface for the P atoms (variable capping ligand–NC bonding environment). This effect is drastically decreased for the coated ones, the ligands being removed from the InP surface. Consequently, upon adding ZnS (this work) or  $\text{InPO}_x$  shell,<sup>16</sup> the broadening effect of the heterogeneous environments at the surface disappears and the narrowing of the  $^{31}\text{P}$  NMR signal is observed.

XPS spectra and relative data of InP/ZnS are respectively presented in Figures 2 and 5 and Table 1. Similarly to InP QDs, the atomic percentage of carbon of InP/ZnS QDs is high (~63%) due to the presence of palmitic acid at the surface of these nanoparticles (Table 1). The C1s core peak presents three components: the first and most intense intensity one (C1:285.0 eV) is attributed to C–C and C–H bonds due to the presence of palmitic acid at the surface of the InP/ZnS QDs (Table 1). The second component, at 286.5 eV, corresponds to C–O bonds (the corresponding O1s component, called O4, is located at 533.3 eV). The last C1s component, located at high binding energy (288.9 eV), is associated with carboxylate function in relation with the corresponding O1s component O3 at 532.1 eV. The In  $3d_{5/2}$  and In  $3d_{3/2}$  peaks are located at 445.4 and 452.9 eV, respectively (Figure 2a, top). These values are shifted to higher binding energies (+0.7 eV) compared to InP QDs sample. This result is also confirmed with the valence band spectrum (Figure 6). For both samples, the valence band spectra show a well-defined peak around 18–19 eV, which is mainly attributed to the ionization of the 4d atoms of indium. For the InP@ZnS sample this peak is shifted to higher binding energies (Figure 6) if we compare with InP, in agreement with the In 3d XPS core peaks. This shift is probably the signature of a modified chemical environment and is consistent with an additional oxidation process during the coating. This assignment is further supported by the P 2p spectrum (Figure 2b, top): the predominant doublet is no longer that of InP (129.0–129.9 eV), but rather that of phosphorus atoms at higher binding energies characteristic of an oxidized environment, such as  $\text{InPO}_x$ -type (133.5–134.4 eV).<sup>20</sup>

XPS is also highly informative to give insight into possible diffusion phenomena and to provide a detailed description of the interface (graded vs abrupt nature) between the core and the ZnS shell. Through a detailed XPS study on QDs prepared with indium carboxylate and  $\text{PH}_3$  as indium and phosphorus

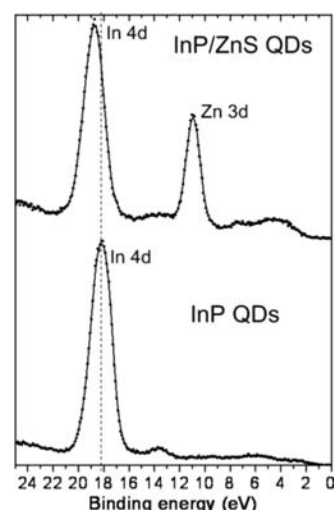


**Figure 6.** XPS valence spectra of InP and InP/ZnS QDs.

sources, Reiss et al.<sup>10,11</sup> showed previously that, according to the synthetic procedures, different internal structures were obtained. A single-step route (i.e., core and shell precursors added at the same time) yielded radially graded InPZnS alloy structure with a thin ZnS shell, while a two-steps approach results in distinct InP and ZnS zones with a graded interface layer. This latter diagnostic relied on the exclusive analysis of the In  $3d_{5/2}$  spectra, and despite the use of high-energy resolution XPS, the In–P–S and In–P–O contributions cannot be distinguished. Indeed, at a first order of interpretation based on the initial state effect, the electronegativity difference between sulfur and oxygen is not large enough to allow discriminating In–P–S and In–P–O from the indium core peak shift. The presence of oxide was ruled out on the basis of the use of inert atmosphere during the synthesis.<sup>15</sup> However, as we have recently demonstrated that the synthesis of InP NCs using carboxylate precursors results in the InP surface partial oxidation due to side reaction involving the carboxylate capping ligands,<sup>16</sup> we can assume today slightly different interpretations.

The S 2p spectrum of the InP/ZnS QDs has been recorded and compared to S 2p spectra obtained for  $\text{In}_2\text{S}_3$  and ZnS (Figure 5a, top). It presents two contributions, the predominant S1 (161.4–162.6 eV), which is associated with  $\text{S}^{2-}$  present in ZnS, and a second one, S2, located at 161.9–163.1 eV (Figure 5a). These binding energies correspond to  $\text{S}^{2-}$  anions. Depending on the ionic character of the  $\text{M}^{n+}\text{--S}^{2-}$  bond in sulfide materials, the  $\text{S}2p_{3/2}$  component for  $\text{S}^{2-}$  anions could be shifted from 163 eV ( $\text{SiS}_2$  compound) to 160 eV ( $\text{Na}_2\text{S}$  compound). The presence of a few percent of In–S bonds could, thus, be envisioned, but this hypothesis appears unlikely when examining the corresponding Auger spectrum of the InP/ZnS QDs (Figure 2d, top). The characteristic signature of  $\text{In}_2\text{S}_3$  (Figure 2d, bottom) is indeed absent and allows us to rule out the presence of significant amounts of In–S. Therefore, the second contribution, S2, which is visible in the S 2p spectrum (Figure 5a, top), is probably a signature of an oxidation of the ZnS shell, either at the surface due to carboxylate ligands (see Table 1, C3 and O3 components) or at the inner interface with the  $\text{InPO}_x$  phase. Finally, regarding the possibility of having large quantities of ZnO at the interfaces, comparison of the O1s spectra of InP/ZnS QDs (Figure 2c) and of the reference of ZnO (Figure S3) clearly demonstrates that, if some ZnO is

formed, it must be in negligible amounts since no peak appears at 530.1 eV (O1 component, Table S2).

To complete the characterization and probe the surface environment of the NCs, a combination of spectroscopic techniques was then employed. The FT-IR spectrum of the as-synthesized InP/ZnS NCs is shown in Figures 7 and S4.

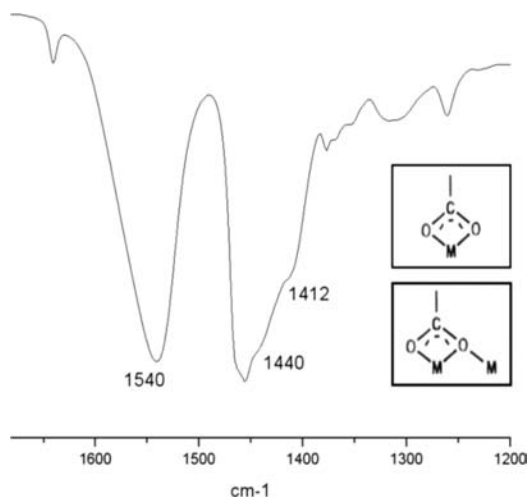


**Figure 7.** Solid-state FT-IR spectrum of the InP/ZnS QDs in the carboxylate stretching frequency range.

It is very reminiscent of the IR spectrum of the InP NCs with, in particular, strong vibrational peaks around 1540 and 1450  $\text{cm}^{-1}$  which are respectively assigned to the antisymmetric and symmetric stretching bands of the carboxylate ligands, i.e., palmitate and undecylenate.<sup>27</sup> Consistently, the CP  $^1\text{H}$ - $^{13}\text{C}$  MAS NMR spectrum (Figure 8) shows, in the carbonyl chemical shift range, the presence of a broad resonance (a width at half-height of 250 Hz) at  $\delta$  183.5 ppm and confirms the role of carboxylate as ligand.

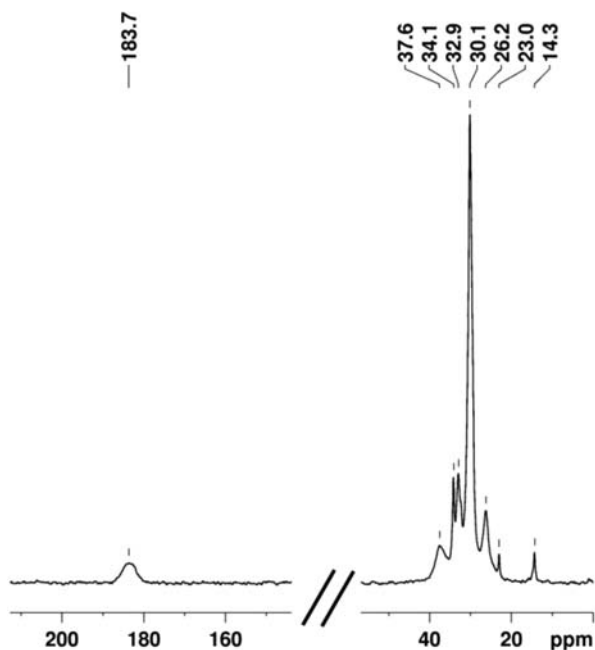


**Figure 8.** CP  $^1\text{H}$ - $^{13}\text{C}$  MAS NMR spectrum of InP/ZnS QDs.

Thanks to the frequency difference between the antisymmetric and symmetric  $\nu(\text{CO}_2^-)$  stretches, ionic and monodentate bonding modes can be ruled out<sup>27</sup> (Figure 9a).

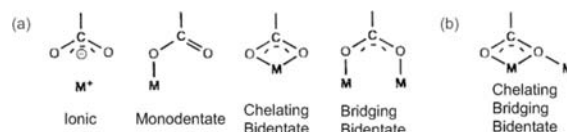


**Figure 9.** (a) Basic carboxylate binding modes and (b) additional carboxylate binding mode observed in indium carboxylate complexes.

However, in the case of zinc compounds, it is not feasible to discriminate the chelating bidentate mode from the bridging bidentate mode only via IR data. Fortunately, the carbonyl chemical shift (183.5 ppm) allows unambiguous assignment to a chelating mode, as the true bridging bidentate mode would have resulted in, at least, a 4 ppm shift.<sup>28,29</sup>

The width of the NMR resonance together with the asymmetry and the width of the antisymmetric and symmetric IR bands may also indicate the possible existence of more than one component, i.e., more than a symmetrically chelating bidentate coordination (Figure 9). A similar dual bonding mode is observed for the unshelled InP NCs.<sup>16</sup>

The ligand/surface interaction was studied using DOSY experiments which allow the determination of the self-diffusion coefficient of the ligand carboxylate. Diffusion coefficients and hydrodynamic radii are correlated by the Stokes–Einstein relation,  $D = kT/6\pi\eta r$  (where  $D$  is the diffusion coefficient,  $k$  is the Boltzmann constant,  $T$  is the temperature in K,  $\eta$  is the viscosity of the solution, and  $r$  is the radius). The self-diffusion coefficient of palmitate has a value of  $3.3 \times 10^{-10} \text{ m}^2/\text{s}$  in InP QDs (Figure S5) and indicates a hydrodynamic radius of 2.4 nm in chloroform. This value is consistent with the size measured by TEM and, thus, shows that these ligands are tightly bound to the NCs surface. Loosely coordinated palmitate would have, indeed, resulted in a higher diffusion coefficient (i.e., close to that of palmitic acid in chloroform,  $6.8 \times 10^{-10} \text{ m}^2/\text{s}$ , Figure S5), as previously evidenced by Martins et al.<sup>30</sup>

To sum up, coating with ZnS unexpectedly leads to an additional oxidation of the InP core. Thus, the InP/ZnS QDs prepared using carboxylate precursors are accurately described as core/double shell nano-objects: the core is an unoxidized crystalline InP phase, and the two coating layers are respectively composed of  $\text{InP}_x\text{O}_y$  and ZnS, with an abrupt interface (no interface diffusion). The capping ligands are carboxylate species tightly bonded at the NCs surface. A graphical schematic representation summarizing the core/multishell structure is given in Figure 10.

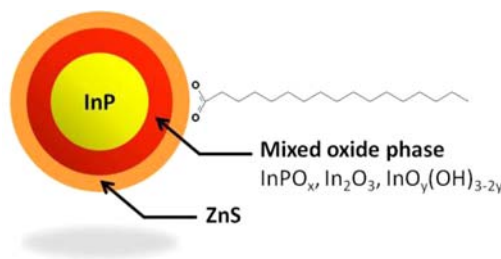


**Figure 10.** Graphical schematic representation of InP/ZnS QDs.

### Precursors' Reactivity and InP Oxidation Mechanism during the Coating Process.

We have previously shown that the decarboxylative coupling of carboxylate (ketone generation), which occurs concomitantly with InP NCs synthesis, yields oxidative conditions and, thus, partial oxidation of the InP QDs surface.<sup>16</sup> Therefore, we have here examined the hypothesis of a similar phenomenon (decarboxylative coupling) during the shelling process. Purified InP NCs (i.e., free of palmitone generated during their own synthesis) were treated according to the coating protocol (zinc undecylenate and elemental sulfur at 230 °C for 1 h). The reaction mixture was analyzed by IR spectroscopy and indeed showed the formation of a ketone (Figure 11). Thus, a decarboxylative coupling of

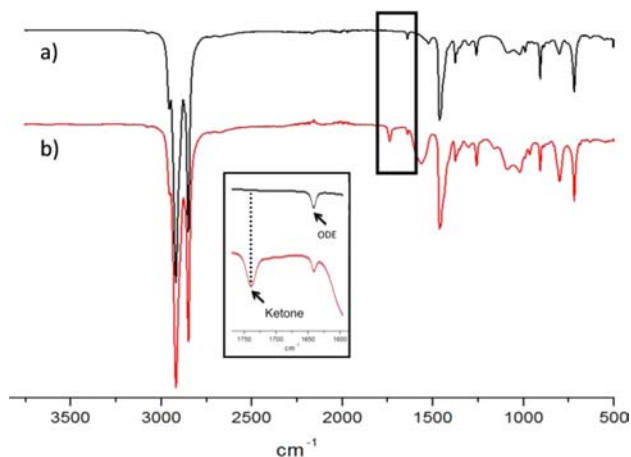


**Figure 11.** FT-IR spectra of (a) purified InP QDs and (b) reaction mixture after ZnS coating. The inset shows the magnification of the spectra in the 1750–1600  $\text{cm}^{-1}$  range.

undecylenate during the coating step can be reasonably assumed, leading to oxidative conditions responsible for the additional oxidation of the InP core. This result supports the generality of ketonization with metal carboxylates at such temperatures. However, the reactivity of zinc carboxylate is different from that of indium carboxylate. Indeed, in contrast to the indium counterpart, no ketone was detected after heating zinc undecylenate alone, in the same conditions as those used for coating (i.e., 230 °C for 1 h). Additionally, treatment of InP QDs with zinc undecylenate (in the conditions of coating) did not either result in oxidation of the InP core, showing unambiguously that oxidation goes along with the formation of the ZnS shell.

Concerning the molecular mechanisms involved during the shelling step, Peng et al. have very recently shown that the active sulfur species in the formation of CdS QDs is not, as initially anticipated, elemental sulfur, but hydrogen sulfide.  $\text{H}_2\text{S}$  results from the activation of  $\text{S}_8$  by ODE. In the second step, the reaction of  $\text{H}_2\text{S}$  with the cadmium carboxylate yields, besides the QDs, carboxylic acids.<sup>31</sup> Given the similarity of our procedure, it is highly probable that our coating step with zinc undecylenate and sulfur in ODE also generates carboxylic acid in the reaction medium, leading then to decarboxylative coupling and ketone formation. In order to test this assumption, we have treated the purified-InP NCs with palmitic acid in the coating conditions. A similar experiment (i.e., InP QDs treated with acetic acid) was previously studied and showed increased QY.<sup>25</sup> This result was interpreted by the authors as etching. However, in our case, the reaction with

palmitic acid results, on one hand, in the formation of palmitone, as evidenced by the IR spectrum of the reaction mixture (Figure S6), and on the other hand, in the additional oxidation of the treated InP QDs. The  $^{31}\text{P}$  NMR spectrum shows that the percentage of unoxidized phosphorus atoms in InP NCs decreases compared to that of untreated InP NCs (65% vs 92%) (Figure S7). This suggests the oxidation of a part of InP and leads to the enlargement of the mixed oxide shell at the expense of the core. The consequence in terms of optical properties is the strong decrease of the intensity of the surface defect emission in favor of the band edge luminescence as the result of the surface passivation.<sup>32</sup>

In summary, the surface of the InP NCs represents a highly reactive zone where decarboxylative coupling occurs easily with metal carboxylates at the temperatures typically used for QDs preparation. The mechanisms involved differ according to the reactants and the steps; however, the inherent *in situ* generation of carboxylate (as anionic ligand or in its acid form) results systematically in oxidation phenomena rather than etching, as previously proposed.<sup>25,26</sup>

## CONCLUSION

This work provides a comprehensive overview of the surface and the interface of the InP/ZnS QDs prepared from indium and zinc carboxylate-based routes. Using a combination of spectroscopic techniques (in particular, XPS, IR, and solution- and solid-state  $^1\text{H}$ ,  $^{13}\text{C}$ , and  $^{31}\text{P}$  NMR) that allows a detailed description of the structure and of the dynamics at the molecular scale, we have shown that these QDs display a complex structure that involves an InP core and several shells of  $\text{InP}_x\text{O}_y/\text{ZnS}/\text{palmitate}$ . The interface between InP and ZnS is a mixed oxide layer that is the consequence of oxidative conditions due to side reactions occurring during the synthesis of the InP core but also during the formation of the ZnS shell. Given the large lattice mismatch that exists between InP and ZnS (7.8%), it is probable that this amorphous interface helps the ZnS shell to grow. However, it can also be at the origin of the moderate QYs observed in the literature. Given the central and ubiquitous role played by zinc sulfide as a biocompatible coating material, the issue of oxidation at the interface deserves particular attention for the understanding and the control of the physical and chemical properties of the as-synthesized core/ZnS QDs. This study provides evidence that the coating procedures may produce unexpected and unwanted effects, which modify dramatically the nature and the surface state of the QDs. It is probable that similar phenomena occur in other coating processes, suggesting that careful examination of molecular processes may be a priority for the development of rational synthesis strategies<sup>33</sup> for controlled nanomaterials. In this respect, future works oriented toward the examination of the potential occurrence of oxidation in nano-objects prepared via single-step procedures<sup>11</sup> (which display superior QY) would be highly desirable in the pursuit of the rationalization and the optimization of QDs (photo)physical properties.

## ASSOCIATED CONTENT

### Supporting Information

Additional figures and experimental details. This material is available free of charge via the Internet at <http://pubs.acs.org>.

## AUTHOR INFORMATION

**Corresponding Author**  
fdelpch@insa-toulouse.fr

## Notes

The authors declare no competing financial interest.

## ■ ACKNOWLEDGMENTS

H.V. and A.C.G. are grateful to the Ministère de l'Enseignement Supérieur et de la Recherche for fellowships. W.-S.O. is grateful to the Université Paul Sabatier for a postdoctoral grant. This work was supported by the Université Paul Sabatier, the Région Midi-Pyrénées, the CNRS, the Institut National des Sciences Appliquées de Toulouse and the European Commission for the POCTEFA Interreg project (MET-NANO EFA 17/08). We thank Yannick Coppel and Christian Bijani for NMR measurements.

## ■ REFERENCES

- (1) Talapin, D. V.; Lee, J.-S.; Kovalenko, M. V.; Shevchenko, E. V. *Chem. Rev.* **2010**, *110*, 389.
- (2) Reiss, P.; Protiere, M.; Li, L. *Small* **2009**, *5*, 154.
- (3) Wang, X.; Ren, X.; Kahen, K.; Hahn, M. A.; Rajeswaran, M.; Maccagnano-Zacher, S.; Silcox, J.; Cragg, G. E.; Efros, A. L.; Krauss, T. D. *Nature* **2009**, *459*, 686.
- (4) Bals, S.; Casavola, M.; van Huis, M. A.; van Aert, S.; Batenburg, K. J.; van Tendeloo, G.; Vanmaekelbergh, D. *Nano Lett.* **2011**, *11*, 3420.
- (5) Tschirner, N.; Lange, H.; Schliwa, A.; Bierman, A.; Thomsen, C.; Lambert, K.; Gomes, R.; Hens, Z. *Chem. Mater.* **2012**, *24*, 311.
- (6) Borchert, H.; Talapin, D. V.; McGinley, C.; Adam, S.; Lobo, A.; de Castro, A. R. B.; Möller, T.; Weller, H. *J. Chem. Phys.* **2003**, *119*, 1800.
- (7) Borchert, H.; Dorfs, D.; McGinley, C.; Adam, S.; Möller, T.; Weller, H.; Eychmüller, A. *J. Phys. Chem. B* **2003**, *107*, 7486.
- (8) Battaglia, D.; Peng, X. *Nano Lett.* **2002**, *2*, 1027.
- (9) Xu, S.; Ziegler, J.; Nann, T. *J. Mater. Chem.* **2008**, *18*, 2653.
- (10) Li, L.; Protiere, M.; Reiss, P. *Chem. Mater.* **2008**, *20*, 2621.
- (11) Li, L.; Reiss, P. *J. Am. Chem. Soc.* **2008**, *130*, 11588.
- (12) Lovingood, D. D.; Strouse, G. F. *Nano Lett.* **2008**, *8*, 3394.
- (13) Gao, J.; Chen, K.; Luong, R.; Bouley, D. M.; Mao, H.; Qiao, T.; Gambhir, S. S.; Cheng, Z. *Nano Lett.* **2012**, *12*, 281.
- (14) (a) Nann, T.; Skinner, W. M. *ACS Nano* **2011**, *5*, 5291. (b) Yang, X.; Zhao, D.; Leck, K. S.; Tan, S. T.; Tang, Y. X.; Zhao, J.; Demir, H. V.; Sun, X. W. *Adv. Mater.* **2012**, *24*, 4180.
- (15) Huang, K.; Demadrille, R.; Silly, M. G.; Sirotti, F.; Reiss, P.; Renault, O. *ACS Nano* **2010**, *4*, 4799.
- (16) Cros-Gagneux, A.; Delpech, F.; Nayral, C.; Cornejo, A.; Coppel, Y.; Chaudret, B. *J. Am. Chem. Soc.* **2010**, *132*, 18147.
- (17) El Hawi, N.; Nayral, C.; Delpech, F.; Coppel, Y.; Cornejo, A.; Castel, A.; Chaudret, B. *Langmuir* **2009**, 7540.
- (18) Massiot, D.; Fayon, F.; Capron, M.; King, I.; Le Calvé, S.; Alonso, B.; Durand, J. O.; Bujoli, B.; Gan, Z.; G. Hoatson, G. *Magn. Reson. Chem.* **2002**, *40*, 70.
- (19) M4N45N45 is relative to the corresponding Auger transition. An Auger electron spectroscopy (AES) transition is written as ABC, where A indicates the level of ionization, B the level where the second electron involved in the transition comes from, and C the level from which the Auger electron is emitted. For A, B, and C, the X-ray notation is used and the AES nomenclature usually follows this X-ray notation: the states with  $n = 1, 2, 3, \dots$  are designated K, L, M, N, ..., while the combinations of  $l$  and  $j$  are given the suffixes 1, 2, 3, ....
- (20) Mohapatra, P.; Dung, M. X.; Choi, J.-K.; Jeong, S.; Jeong, H.-D. *Bull. Korean Chem. Soc.* **2011**, *32*, 263.
- (21) Donley, C.; Dunphy, D.; Paine, D.; Carter, C.; Nebesny, K.; Lee, P.; Alloway, D.; Armstrong, R. *Langmuir* **2002**, *18*, 450.
- (22) Bergignat, E.; Hollinger, G. *Surf. Sci.* **1987**, 189–190, 353.
- (23) Nelson, A.; Geib, K.; Wilmse, C. W. *J. Appl. Phys.* **1983**, *54*, 4134.
- (24) Xie, R.; Battaglia, D.; Peng, X. *J. Am. Chem. Soc.* **2007**, *129*, 15432.
- (25) Ryu, E.; Kim, S.; Jang, E.; Jun, S.; Kim, B.; Kim, S.-W. *Chem. Mater.* **2009**, *21*, 573.
- (26) Zhan, F.; Ren, J. *J. Mater. Chem.* **2012**, *22*, 1794.
- (27) Nakamoto, K. *Infrared and Raman Spectra of Inorganic and Coordination Compounds*; Wiley-Interscience: New York, 1978; p 232.
- (28) Ye, B.-H.; Li, X.-Y.; Williams, I. D.; Chen, X. M. *Inorg. Chem.* **2002**, *25*, 6426.
- (29) Demsar, A.; Kosmrlj, J.; Petricek, S. *J. Am. Chem. Soc.* **2002**, *124*, 3951.
- (30) Fritzing, B.; Moreels, I.; Lommens, P.; Koole, R.; Hens, Z.; Martins, J. C. *J. Am. Chem. Soc.* **2009**, *131*, 3024.
- (31) Li, Z.; Ji, Y.; Xie, R.; Grisham, S. Y.; Peng, X. *J. Am. Chem. Soc.* **2011**, *133*, 17248.
- (32) (a) Guzelian, A. A.; Katari, J. E. B.; Kadavanich, A. V.; Banin, U.; Hamad, K.; Juban, E.; Alivisatos, A. P.; Wolters, R. H.; Arnold, C. C.; Heath, J. R. *J. Phys. Chem.* **1996**, *100*, 7212. (b) Protière, M.; Reiss, P. *Chem. Commun.* **2007**, 2417.
- (33) (a) Owen, J. S.; Chan, E. M.; Liu, H.; Alivisatos, A. P. *J. Am. Chem. Soc.* **2010**, *132*, 18206. (b) Cossairt, B. M.; Owen, J. S. *Chem. Mater.* **2011**, *23*, 3114. (c) Allen, P. M.; Walker, B. J.; Bawendi, M. G. *Angew. Chem., Int. Ed.* **2010**, *49*, 760. (d) Hugues, B. K.; Luther, J. M.; Beard, M. C. *ACS Nano* **2012**, *6*, 4573.